Title: Two-Dimensional High-Entropy Transition Metal Dichalcogenides for Carbon Dioxide Electrocatalysis

Authors: John Cavin[1#], Alireza Ahmadiparidari[2,#], Leily Majidi[2], Arashdeep Singh Thind[3], Saurabh N. Misal[2], Aditya Prajapati[4], Zahra Hemmat[2], Sina Rastegar[2], Andrew Beukelman[5], Meenesh R Singh[4], Kinga A. Unocic[6], Amin Salehi-Khojin[2*], Rohan Mishra[5,3*]

Affiliations:

[1]Department of Physics, Washington University in St. Louis, St. Louis, MO 63130, USA.

[2]Department of Mechanical and Industrial Engineering, University of Illinois at Chicago, Chicago, IL, 60607, USA.

[3]Institute of Materials Science and Engineering, Washington University in St. Louis, St. Louis, MO 63130, USA.

[4]Department of Chemical Engineering, University of Illinois at Chicago, Chicago, IL, 60607, USA.

[5]Department of Mechanical Engineering and Material Science, Washington University in St. Louis, St. Louis, MO 63130, USA.

[6]Center for Nanophase Materials Sciences, Oak Ridge National Laboratory, Oak Ridge, TN 37830, TN, USA.

[#]These authors contributed equally to this work.

*Correspondence and requests should be addressed to A.S.-K. (salehik@uic.edu) or R.M.(rmishra@wustl.edu).

Abstract:

High-entropy alloys combine multiple principal elements at a near equal fraction to form vast compositional spaces to achieve outstanding functionalities that are absent in alloys with one or two principal elements. Here, the prediction, synthesis, and multiscale characterization of two-dimensional (2D) high-entropy transition metal dichalcogenide (TMDC) alloys with four/five transition metals is reported. Of these, the electrochemical performance of a five-component alloy with the highest configurational entropy, $(MoWVNbTa)S_2$, is investigated for CO_2 conversion to CO, revealing an excellent current density of 0.51 A/cm^2 and a turnover frequency of 58.3 s^{-1} at ~-0.8 V vs RHE. First-principles calculations show that the superior CO_2 electroreduction is due to a multi-site catalysis wherein the atomic-scale disorder optimizes the rate-limiting step of CO desorption by facilitating isolated transition metal edge sites with weak CO binding. 2D high-entropy TMDC alloys provide a materials platform to design superior catalysts for many electrochemical systems.

Main Text:

The incorporation of many principal elements into the so-called high entropy alloys (HEAs) has generated significant interest since their first report in 2004.[1] As opposed to traditional multicomponent alloys, which include one or two principal elements with others at lower fractions, HEAs contain multiple elements at the near equimolar fraction. They provide a vast combinatorial space for the design of new materials with outstanding functionalities that remains largely unexplored. More recently, the field of HEAs has been expanding beyond metal alloys to include metal-oxides,[2] nitrides,[3] carbides,[4] borides[5] and silicides[6] with the aim of achieving superior mechanical properties.[7] However, reports on two-dimensional (2D) HEAs that can blend the

combinatorial properties of HEAs with the physical properties of 2D materials that are attractive to applications like electrocatalysis, such as their large surface area, are missing.

Here, we present a successful synthesis of layered high-entropy transition metal disulfides involving alloying of 4 – 5 transition metals from group IV and V of the Periodic Table. The relative stability of these high-entropy transition metal dichalcogenides (TMDCs) was quantified using density-functional-theory (DFT) calculations of formation enthalpy together with the change in configurational entropy upon alloying to estimate the growth temperature above which the HEA is stable against decomposition. We predict four alloys, $(MoWNbV)S_2$, $(MoWNbTa)S_2$, $(MoWVNbTa)S_2$, and $(MoVNbTa)S_2$, to be stable at relatively low growth temperatures. Subsequently, we have successfully synthesized the first three of these alloys with approximately equimolar stoichiometries and found that the $(MoWVNbTa)S_2$ HEA shows an exceptionally high electrocatalytic performance for CO_2 conversion.

We restricted our screening and synthesis attempts to equimolar sulfide alloys of Mo, W, V, Nb and Ta because their unary sulfides exist in the triangular prismatic *2H* phase. Furthermore, we chose equimolar compositions where entropy stabilization is maximized and can enhance the stabilization of the alloy. Eight of the ten possible binary alloys of these TMDCs have a positive mixing enthalpy and are, hence, immiscible at lower temperatures.[8] However, they can be stabilized in single-phase solid solutions by growing them at higher temperatures where the configurational entropy, which favors miscibility, dominates the contribution to the Gibbs free energy (ΔG). We refer to the minimum growth temperature above which the alloy is miscible as its miscibility temperature T_{misc}, which can be calculated using first-principles methods, as has been shown for binary alloys in a recent work.[8]

HEAs take advantage of the increase in configurational entropy due to the large number of components to stabilize a single-phase solid solution, even though pairwise alloys of the components might be immiscible. But because the number of required calculations to determine T_{misc} scales exponentially with the number of alloy components, this method is intractable for HEAs. Instead, we introduce an easy to calculate temperature T_0, that assesses the stability of HEAs relative to individual and binary components for a specific composition and use it to estimate T_{misc}. Using the enthalpies of pairwise binary alloys to predict the stability of HEAs is a popular technique;[9] our method expands on this by also including the enthalpy of the equimolar HEA. Furthermore, all the TMDC HEAs we studied have delocalized electrons at the Fermi energy (see Figure S1 in the Supplemental Information).[10] We define T_0 for an equimolar HEA as the temperature above which ΔG of the solid solution is lower than that of all possible decompositions into mixtures of unary TMDCs and equimolar binary TMDC alloys. Computational details provided in the Experimental Section and details regarding the screening method are provided in the Supporting Information (Section S5). While calculating T_{misc} of an N-component alloy requires sampling the mixing enthalpy of an (N-1)-dimensional composition space, calculating T_0 only requires the mixing enthalpy corresponding to equimolar binary alloys of the TMDCs being alloyed.

To illustrate how T_0 is calculated, we show the process for $(MoWNbV)S_2$, which we abbreviate as (Mo,W,Nb,V). The mixing enthalpies at multiple molar concentration values for the six possible binary alloys are plotted in Figure 1A. From this plot, we see that (Mo,W) is the only pairwise alloy with a negative mixing enthalpy and is expected to be miscible at any temperature. All the other pairwise binary alloys are immiscible at lower temperatures, which makes (Mo,W,Nb,V) a good case study to demonstrate how stability can be improved by adding more

components. To show the relation between T_0 and T_{misc}, Figure 1B shows ΔG of the (V,Nb) alloy at $T = 0$ K, T_0, and T_{misc}. The alloy (V,Nb) is chosen for its relevance to the four-component alloy (Mo,W,Nb,V). At T_0, $\Delta G = 0$ at $x = 0.5$ as per its definition; at T_{misc}, ΔG is concave up, meaning the disordered alloy is stable against phase separation. This procedure was repeated for the other five pairwise binary alloys, and the resulting T_0 and T_{misc} are shown in Figure 1C as shaded and unshaded bars, respectively. For each alloy, $T_0 < T_{misc}$, and there is a strong correlation between T_{misc} and T_0 (Figure S2, Supporting Information) with the exception of (Mo,Nb), which has a large asymmetric mixing enthalpy (Figure 1A) that leads to a high T_{misc} with a relatively low T_0.

To determine T_0 for (Mo,W,Nb,V), ΔG of all possible decomposition products (see Table S1) and the HEA are plotted as a function of temperature. At each temperature, the phase mixture with the lowest energy is "stable" by our criterion. Figure 1D shows the Gibbs free energy versus temperature for all phase mixtures that are, for some range of temperature, most stable. The solid, piece-wise line corresponds to the ground state —amongst the various phases considered here— at each temperature. Between 0 – 480 K, the ground state comprises of (Mo,W)+(Nb)+(V), followed by a mixture of (Mo,W)+(Nb,V) between 480 – 540 K. With increasing temperature above 540 K, the HEA becomes stable. This value corresponds to the dashed line in Figure 1C and is lower than T_0 of two of the binary alloys (W,V) and (Mo,V). This shows that while VS_2 does not like alloying with other TMDCs, entropy-stabilization through the mixing of many components can stabilize TMDC alloys with V.

Figure 1E shows atomic models of the two stable partial decompositions followed by the fully incorporated HEA. The supercell models used in the calculations are shown in Figure S3. Using this procedure, we find T_0 for (Mo,V,Nb,Ta), (Mo,W,Nb,Ta), and (Mo,W,V,Nb,Ta) to be 440 K, 440 K and 740 K, respectively (see Figure S4 for free energy vs temperature plots similar

to Figure 1D and Table S2 for T_0 values, Supporting Information). Estimating the miscibility temperature from the fit in Figure S2 gives 920 K, 920 K and 1220 K respectively. While these estimates are approximate, they suggest that these HEAs can be stabilized by growing them at achievable temperatures (~1,000ºC). Despite having higher entropy, (Mo,W,V,Nb,Ta) is predicted to have a higher T_0 value than the 4-component alloys. This is partially because of the higher mixing enthalpy, and also because of the higher entropy of its most stable partial decomposition products (Mo,W)S_2 and (Nb,Ta)S_2, which results in a smaller difference in entropy between the products and the reactants (see Figure S4).

To verify the stability predictions, we synthesized three out of the four predicted HEAs (see the Experimental Section). Here, we focus on the five-component (Mo,W,V,Nb,Ta) alloy having the highest configurational entropy. The synthesis was carried out using the chemical vapor transport (CVT) method in a single zone furnace followed by a liquid phase exfoliation technique to produce nanoflakes (NFs)of the synthesized materials (details in the Experimental Section). The formation of layered NFs was confirmed by measuring the dimensions of single flakes through atomic force microscopy (AFM, Figure S5) and with scanning transmission electron microscopy high-angle annular dark-field (STEM-HAADF) images from the side of the exfoliated flakes, which show the presence of 8-16 layers (Figure S6). Figure 2A shows the frequency distribution of the principal elements collected from up to 60 NFs using scanning electron microscopy-energy dispersive x-ray spectroscopy (SEM-EDS). We observe only a small deviation from the equimolar ratios used for the synthesis (~6.6 atomic percent) with a richer Mo content and a reduced concentration of V. Figure 2B demonstrates SEM-EDS mapping of principle elements confirming a homogeneous spatial distribution of each element (SEM-EDS mapping for the rest of alloys in Figure S7, Supporting Information).

To further characterize the structure and composition of these flakes at the atomic scale, we have used aberration-corrected STEM combined with EDS analysis (see the Experimental Section). Figure 2C shows the STEM HAADF image of a typical multilayer (Mo,W,V,Nb,Ta) flake. The elemental EDS mapping, as shown in Figure 2D (see Section S1 and Figures S8 and S11, Supporting Information), show sulfur and alloyed transition metals distributed throughout the flake with no evidence of phase segregation. While there are local inhomogeneities in the elemental distribution, they are not systematic or universal across flakes. This assessment is supported by composition comparisons for different regions of the flake shown in Figure 2C and another flake in Figures S9 and S10. Figure 2E shows an atomic resolution HAADF image obtained near the edge of a (Mo,W,V,Nb,Ta) flake, with Figure 2F showing a magnified HAADF image of a region highlighted in Figure 2E. In a HAADF image, the intensity of an atomic column is approximately proportional to the squared atomic number ($\sim Z^2$) of the elements in the column.[11] Figure 2G shows the variation in the intensity of the atomic columns along a vertical line obtained from Figure 2F. The heaviest elements, W and Ta, appear brightest, followed by Mo and Nb, then V, with the S columns having the lowest intensity. To assign the atomic composition for each column in Figure 2F, we have performed STEM-HAADF image simulations, details of which are provided in the Experimental Section. We find that the simulated HAADF image for a 5-layer ABC-stacked TMDC structure with the *3R* phase agrees best with the experimental HAADF image. For the 5-layer ABC-stacked TMDC structure that we have generated, there are three types of atomic columns along the incident electron beam, I = (TM-S-S-TM), II = (S-S-TM-S-S) and III = (S-S-TM-S-S-TM), where each TM-site is chosen from V, Nb, Mo, Ta or W, such that all possible TM permutations are included in the structure. We then assigned the atomic composition of each column in the experimental image (Figure 2F) based on the best match with

simulated HAADF image (see Figure S12 and Figure S13, Supporting Information). STEM-HAADF intensity analysis further confirms the random distribution of the elements in the high entropy TMDC alloy.

Next, we performed CO_2 electrochemical experiments using (Mo,W,V,Nb,Ta) NFs as the cathode catalyst and compared the results with Ag nanoparticles (NPs) under identical experimental conditions and similar nanoparticle average size (see Figure S14). The experiments were performed in a CO_2-saturated aqueous medium of 1 M KOH-1 M choline chloride (see the Experimental Section). This hybrid electrolyte was selected due to the increased ionic conductivity and suppression of hydrogen evolution reaction (HER) due to the addition of choline chloride.[12] The electrolyte is also stable in the applied potential range.[13] The initial pH of choline chloride/KOH (1:1 M) solution is ~13.3, which drops to ~7.6 after CO_2 saturation due to the formation of bicarbonate ions. A previous study revealed that (bi)carbonate ions and CO_2 molecules can participate in a low barrier CO_2 exchange process to supply sufficient reactants (enhanced CO_2 transport) for the electrochemical reactions at the TMDC surface.[13] All electrochemical tests were performed in a custom made two compartment cell separated by Nafion 115 membrane. The three-electrode setup consists of $Ag/AgNO_3$ and Pt as the reference and counter electrode, respectively. First, linear sweep voltammetry (LSV) tests were conducted on both (Mo,W,V,Nb,Ta) NFs and Ag NPs coated on a gas diffusion layer at the scan rate of 50 mV s^{-1}. As illustrated in Figure 3A, the current density for the (Mo,W,V,Nb,Ta) NFs at -0.8 V vs RHE is over 10 times higher than that of Ag NPs reaching up to ~510 mA cm^{-2} normalized based on electrode's geometrical surface area.

To detect the gaseous products online, the cell was directly connected to a differential electrochemical mass spectrometer (DEMS) (See Experimental Section and Figure S15,

Supporting Information). The inset of Figure 3A shows the gaseous products evolved during LSV experiments performed at a scan rate of 1 mV s^{-1}. The DEMS results show formation of CO with a small onset potential of –0.129 V vs RHE (only 19 mV overpotential).[14] Moreover, CO remains the dominant gaseous product up to ~ –0.4 V vs RHE at which H_2 evolution gradually increases (Figure S16, Supporting Information).

Chronoamperometry (CA) experiments were also performed using (Mo,W,V,Nb,Ta) NFs at different potentials in the same setup. The experiments were performed at seven different potentials for 1-hour (Figure S17, Supporting Information). Figure 3B shows that Faradic efficiency (FE) for the formation of CO is ~ 95% at –0.16 V vs RHE and more than 92% at –0.23 and –0.31 V vs RHE. This value starts to drop at ~ –0.4 V vs RHE and is measured to be 72% at –0.76 V vs RHE. On the other hand, FE for H_2 evolution is negligible up to ~-0.4 V vs RHE. After this potential, FE for H_2 evolution starts to increase and reaches ~18% at -0.76 V vs RHE. To detect and quantify possible liquid products, high performance liquid chromatography (HPLC) was used (see the Experimental Section and Figures S20 and S21 and Table S4, Supporting Information). HCOOH was found to be the major liquid product starting at -0.4 V vs RHE (Table S5, Supporting Information). The average FE for HCOOH formation is ~ 13% for the potential window of -0.4 V to -0.61 V vs RHE while this value is calculated to be ~9% at -0.76 V vs RHE. Moreover, to exclude the possibility of product formation (CO and H_2) due to salts decomposition and electrolyte degradation, NMR experiments were conducted before and after 10 hours of operation (see the Experimental Section). NMR results (Figure S22, Supporting Information) show no degradation within the electrolyte after the long-term operation, suggesting that the CO and HCOOH products are formed due to CO_2 reduction.

Turnover numbers (TON) of CO formation over an hour were also calculated based on previously reported methods (electrochemically active surface area resolved)[15] and are shown in Figure 3C (see the Experimental Section and Table S6, Supporting Information). These results indicate that the TON value reaches a maximum of ~209,885 at –0.76 V vs RHE. The turnover frequency (TOF) values at the potential range of –0.16 to –0.76 V vs RHE are shown in the inset of Figure 3C. The TOFs for CO formation at –0.16, –0.23 and –0.31 V vs RHE are 7.13, 21.32 and 32.65 s^{-1}, respectively, which are the highest values among the state-of-the-art catalysts reported so far.[13, 16] In particular, the TOF is 58.30 s^{-1} at –0.76 V vs RHE for the (Mo,W,V,Nb,Ta) NFs, which is more than ~28 times higher compared to that for Ag NPs (2.08 s^{-1}) tested under identical conditions.

To evaluate the long-term stability of the catalyst, extended Chronoamperometry tests (20 hours) were performed at 2 different potentials. As shown in Figure 3D the catalysts stay active at long operation times without a noticeable drop in the current density.

To gain more insight about the remarkable catalytic activity of (Mo,W,V,Nb,Ta) NFs, especially at low overpotentials, we carried out DFT calculations to determine the free energy changes at possible active sites of (Mo,W,V,Nb,Ta) nanoribbons and study the corresponding reaction pathways (Section S6, Supporting Information). These free energies were determined using the computational hydrogen electrode approach at the equilibrium potential where the free energy of the products and the reactants are the same (Section S6, Supporting Information).[17] Figure 4A shows an illustration of each step of the CO_2 reduction reaction at an example transition metal site, in this case V, at the edge of a (Mo,W,V,Nb,Ta) nanoribbon. Metal sites at transition-metal terminated edges are known to be the sites for CO_2 reduction from previous studies on pure TMDCs in ionic liquids.[16b, 18] To capture the effect of different nearest-neighbor coordination on

the catalytic activity of each transition metal active site,[19] four different nanoribbon configurations of this HEA, labeled Ribbon-00-03, were studied (Section S7 and Figure S23, Supporting Information). Using multiple nanoribbon configurations allows us to take configurational averages and ensure our results are reliable and not specific to a single configuration.

The free energies of the reaction steps are shown in Figure 4B for the five different transition metal sites in (Mo,W,V,Nb,Ta). We found CO desorption to be the rate-limiting step for all studied metal sites consistent with the previous report on WSe_2 nanoflakes.[16b] Because of its importance, the binding energy of CO* adsorbate to different metal sites was calculated for all the four nanoribbon configurations. The free energies corresponding to COOH* and CO* absorption on (Mo,W,V,Nb,Ta) in Figure 4B are represented by peaked distributions centered on averages over the four ribbon configurations (see Figure S24 for free energies along the reaction pathways of each configuration individually, Supporting Information). These distributions show how binding energies at transition metal sites vary depending on the local environment. On average, these results indicate that V and Nb sites tend to have lower CO desorption energies compared to W and Mo sites that bind strongly.

For comparison, we included in Figure 4B the free energy pathways for MoS_2 and VS_2, which are the two pure TMDCs having the most extreme energies for CO desorption as well as previous calculations on Ag slabs and NPs.[16b] As discussed above, different local configurations in (Mo,W,V,Nb,Ta) result in a distribution of states for binding with different reaction intermediates (COOH* and CO*). We found the vast majority of CO desorption energies at the varying sites of (Mo,W,V,Nb,Ta) have a smaller average value of 1.08 ± 0.36 eV than MoS_2 (1.55 eV) and is therefore less rate-limiting (see Tables S7 and S8 and Figure S25 for adsorption energy

data and visualization, respectively). We note that these desorption energies are higher than that of VS_2 (0.5 eV). However, because COOH* adsorption is an endothermic electron transfer process on VS_2, it is expected to have a larger overpotential (~100 meV) than (Mo,W,V,Nb,Ta). Similarly, Ag NP catalysts have a large overpotential (~400 meV) due to their weak bonding to COOH*.[16b] Thus, (Mo,W,V,Nb,Ta) benefits from the disordered presence of multiple transition metal atoms that optimize the bonding strength to reduce desorption energy while keeping the overpotential minimal. While a similar effect could be possible in a quasi-binary alloy of VS_2 and MoS_2 or WS_2, previous results show that such quasi-binary alloys have large miscibility gaps;[8] thus, the increase in configurational entropy upon including many principal components is important for stabilizing a TMDC alloy with V and group VI transition metals.

In addition to the small average CO desorption barrier in (Mo,W,V,Nb,Ta), there is also evidence that individual transition metal edge sites will have exceptionally low barriers. Figure S26 in the Supplementary Information shows examples of V and Nb sites with CO desorption energies ranging from 0.5-0.75 eV. These sites have a lower CO desorption energy than the average by about 0.25-0.5 eV. Because activity rates vary exponentially with the energy of these barriers, catalytic activity will be dominated by fast turnover at the weakly binding sites. We also investigated the possibility of CO site hopping using climbing image nudged elastic band to find the minimum energy pathway.[20] The results are shown in Figure S26 for configuration Ribbon-01, where W and Mo are the two "strongest" sites and neighbor V, the "weakest" site having a desorption energy of 0.53 eV (see Figure S24 and S25, Supporting Information). While the hopping of CO from Mo or W to V is favored over direct desorption, the ability to hop back to the strongly bound site precludes any increase in the turnover frequency. However, if the rate of CO_2 capture on strongly bound sites is high enough, hopping could play a role: a CO hopping to a weak

site may not hop back if the strong site has already been filled. We plan to investigate the various catalytic pathways of CO_2 reduction on these TMDC alloys in future using kinetic Monte Carlo methods.

In summary, we have developed a new platform for materials involving 2D high entropy TMDC alloys. This platform can be expanded in future by including non-equimolar compositions with enhanced stability and electrocatalytic properties. Here, we computationally predicted and subsequently synthesized the first near-equimolar 2D high entropy TMDC alloys. The HEA with the highest configurational entropy, $(MoWVNbTa)S_2$, was tested for CO_2 electroreduction. It was shown that this catalyst exhibits extremely high activity with high selectivity towards CO production at low overpotentials. We attribute the high activity of the tested HEA to CO desorption dominated by a minority of weakly binding transition metal edge sites. Owing to these excellent properties, we anticipate high entropy TMDC alloys to have high activity for other core electrocatalytic reactions and open a new pathway for advances in electrochemical energy systems.

Experimental Section

Computational details: Disordered alloys were simulated using special quasi-random structures (SQS's)[21] that were generated using the Alloy Theoretic Automated Toolkit (ATAT).[22] Binary alloys, 4-component alloys, and the 5-component alloy, were studied using 6×6 supercells, 8×8 supercells, and a 65 formulae unit monoclinic supercell, respectively, as shown in Figure S3. Ribbons were constructed with 5-unit cells along their periodic direction and 6 layers of transition metals along their lateral direction for a total of 30 formula units. All calculations were performed on monolayer structures with the expectation that they would generalize to bulk TMDCs due to the weak inter-layer coupling. A vacuum spacing of >15 Å was used to reduce the interaction between image planes and/or ribbons due to the use of periodic boundary conditions. Total

energies were calculated using DFT as implemented in VASP using the Perdew-Burke-Ernzerhof exchange-correlation functional.[23] For the large SQS's, geometric relaxation was conducted at only the Γ-point in the reciprocal space. A subsequent static calculation for electronic structure was performed using a $3 \times 3 \times 1$ *k*-points mesh generated using the Monkhorst-Pack method.[24] A kinetic energy cutoff of 450 eV was used for all the calculations. Additional details on the procedures used to screen the HEAs, calculate the energy barriers for CO_2 reduction reaction on nanoribbons with different configuration and their passivation are provided in the supporting information file.

Synthesis of the high entropy TMDC alloys: Firstly, quartz tubes with inner and outer diameters of 11 and 15 cm, respectively, were etched with 2% HF solution followed by a 24-hour annealing at 1000 ^{0}C. Thereafter, element powders were weighed and added to the tube. The sealing process of the tubes was done under 10^{-5} Torr vacuum pressure. Finally, tubes were placed in a single zone tube furnace and T was chosen to be ramped until it reached T_0 at a rate of 1^{o}C/min for each designated HEA. Then it was heated for 120 hours before it was left to cool down to room temperature at 1^{o}C/min.

STEM experiments and image simulation: STEM imaging was performed using aberration-corrected Nion UltraSTEM^{TM} 200 microscope at Oak Ridge National Laboratory operating at 200 kV. Before imaging, the TEM grids were heated to 160 ºC in vacuum for 8 hours to remove excess solvent and contamination. HAADF images were smoothed using gaussian blurring to accurately determine the atomic positions of atomic columns. The EDS measurements shown in Figure 2C and 2D were performed using FEI Talos F200X S/TEM microscope operating at 200 kV equipped with an extreme field emission gun (X-FEG) electron source and Super-X EDS detector system that includes four silicon-drift detector (SDD) (Bruker XFlash 120 mm^2) units with a solid angle

of 0.9 Steradian for chemical analysis). The EDS detectors are arranged symmetrically around the sample. The elemental hypermaps were acquired with a nominal beam current of 90 pA.

STEM-HAADF simulations were performed using the multi-slice method as implemented in μSTEM.[25] Thermal scattering was included through the phonon excitation model proposed by Forbes et al.[26] The defocus value was tuned to -17 Å to obtain intensity profiles consistent with experimental data. An aberration-free probe with an accelerating voltage of 200 kV and a convergence semi-angle of 30 mrad were used. The inner and outer collection angles for the HAADF detector were set to 80 and 220 mrad, respectively.

Differential electrochemical mass spectroscopy (DEMS): Real time analysis of the gas products from CO_2 reduction was done through DEMS using Hiden Analytical HPR-40 system. CO and H_2 gases were calibrated by detecting 1%, 5%, 10% and 20% of both the gases with Ar in DEMS (Figure S15, Supporting Information). Number of moles (n) of CO and H_2 were calculated by using ideal gas law. Different percentage of the gases were purged in a fixed volume at a constant pressure which gave n of CO (n_{CO}) and n of H_2 (n_{H_2}). These values were compared with difference in partial pressure on DEMS.

High-performance liquid chromatography (HPLC): The liquid products of CO_2 reduction reaction were quantified using HPLC on an Agilent Infinity 1260 II HPLC with a $300mm \times 7.5mm$ Agilent Hi-plex- H column and a refractive index detector (RID). The isocratic elution flow rate of the mobile phase containing 1mM H_2SO_4 was 0.6 mL/min. The column temperature was 60 ^oC, and the RID temperature was 35 ^oC. A 10 μL of the sample was injected into the column through an autosampler and the products were analyzed for a retention time of up to 30 mins. This operating method was developed by observing the retention times of the

electrolyte (KOH and Choline Chloride) and resolving the peaks for possible CO_2 reduction products: HCOOH, HCHO, CH_3OH, CH_3COCH_3, CH_3COOH, C_2H_5OH, and $C_2H_2O_4$.

Atomic Force Microscopy (AFM): AFM topography images were obtained using Bruker Dimension Icon AFM with ScanAsyst-tapping mode.

Dynamic Light-Scattering Measurement (DLS). Measurements of the lateral size of the flakes were performed using the Malvern Zetasizer Nano ZSP system at 25 °C. A 10 mW semiconductor laser with 633 nm emission is used in this instrument.

Nuclear Magnetic Resonance (NMR) spectroscopy: The NMR samples from 1M KOH: 1M choline chloride were prepared by adding 0.1 mL electrolyte to 0.9 mL D_2O. 5 mm NMR glass tubes. ^1H NMR and ^{13}C NMR experiments were carried out with a Bruker Advance III 500 MHz system equipped with DCH cryoprobe at Integrated Molecular Structure Education and Research Center (IMSERC) at Northwestern University, to assess the stability of the electrolyte before and after the experiments. The NMR experiments were carried out at 298 K.

Electrochemical reduction of CO_2: All of the electrochemical tests were carried out by Voltalab potentiostat (PGZ100). 1 M choline chloride ($C_5H_{14}CINO$, Sigma-Aldrich) and 1 M potassium hydroxide (KOH, Fisher-Scientific) in aqueous media (pH ≈ 7.6 after CO_2 purge and saturation) were used as the electrolyte for electrochemical reduction of CO_2. The high concentration of the supporting electrolyte helped to remove migration effects. For CV experiments a premixed solution was used by purging of CO_2 for 30 min until it was saturated. CA experiments were conducted by constantly purging CO_2 into the system to avoid CO_2 deficiency and maintaining constant pH during experiments. A two-compartment cell was used for linear sweep voltammetry (LSV) and chronoamperometry experiments. $(MoWNbTaV)S_2$ and Ag were exfoliated by liquid phase exfoliation method.[16b, 27] In detail, 0.3 grams of synthesized HEA

powder was mixed with 80 mL of isopropyl alcohol and was ultra-sonicated with 7 watts power in an ice bath surrounding for 20 hours. Next, the collected solution was centrifuged at 2000 RPM speed for one hour before the top 80% supernatant was collected. The exfoliated high entropy alloy nanoflakes (NFs), and Ag nanoparticles (NPs) were drop cast on a 0.2×0.2 cm^2 (to minimize the mass transfer issues due to high turnover number of CO_2 reduction in our catalyst) gas diffusion layer (Sigracet 25BC, purchased from FuelCellsEtc) until it reached 0.2 mg/cm^2 loading. $Ag/AgNO_3$ was used as a reference electrode and Platinum wire (surface area 0.48 cm^2) was used as counter electrode. Potentials were converted to RHE using: V vs RHE = V vs $Ag/AgNO_3$ + 0.155 + 0.0592*pH. The reported potentials were iR corrected. LSV experiments were performed with $MoWNbTaVS_2$ NFs at scan rate of 50 mV s^{-1} and performance was compared with Ag NPs. A two-compartment cell was used when the products were analyzed for chronoamperometry experiments and LSV experiments at scan rate of 1 mV s^{-1}. pH of the solution was measured at the end of the chronoamperometry experiments.

Data and Materials Availability: All data is available in the main text or in the supplementary information file.

Supporting Information

Supporting Information is available from the Wiley Online Library or from the author

Acknowledgments

A portion of the STEM experiments was conducted at the Center for Nanophase Materials Sciences at Oak Ridge National Laboratory, which is a Department of Energy (DOE) Office of Science User Facility, through a user project. STEM-EDS microscopy research was supported by the Office of Nuclear Energy, Fuel Cycle R&D Program and the Nuclear Science User Facilities. This work used the computational resources of the Extreme Science and Engineering Discovery

Environment (XSEDE), which is supported by NSF ACI-1548562. Authors would also like to acknowledge NUANCE at Northwestern University for their resources. **Funding:** This work was supported by National Science Foundation (NSF) DMREF 1729420 and NSF-CBET 1800357 (A.AP, S.M., Z.H., A.S.-K.) and NSF-DMREF 1729787 (J.C., A.B. and R.M.). A.S.T. was supported by NSF DMR-1806147. R.M. further acknowledges partial support through NSF DMR-1809571.

Conflict of Interest

The authors declare no conflict of interest.

Author Contributions

J.C. and A.A. contributed equally to this work. R.M., A.S.-K., J.C., and A.A. conceived the project and wrote the manuscript. J.C., A.B. and R.M. performed the theoretical calculations. A.A. and Z.H. synthesized materials. A.A., S.N.M and L.M. performed electrochemical tests and calculations. Z.H. performed the EDS mapping of NFs. A.P. and M.R.S. performed and supervised HPLC testing. A.S.-K. supervised the material synthesis and electrochemical experiments. A.S.T. performed the STEM experiments and analysis with assistance from K.A.U., J.C. and R.M. All the authors discussed the results and contributed to the revision of the manuscript.

References

[1] a) B. Cantor, I. T. H. Chang, P. Knight, A. J. B. Vincent, *Materials Science and Engineering a-Structural Materials Properties Microstructure and Processing* **2004**, *375*, 213; b) J. W. Yeh, S. K. Chen, S. J. Lin, J. Y. Gan, T. S. Chin, T. T. Shun, C. H. Tsau, S. Y. Chang, *Adv Eng Mater* **2004**, *6*, 299.

[2] C. M. Rost, E. Sachet, T. Borman, A. Moballegh, E. C. Dickey, D. Hou, J. L. Jones, S. Curtarolo, J.-P. Maria, *Nature Communications* **2015**, *6*, 8485.

[3] M.-H. Hsieh, M.-H. Tsai, W.-J. Shen, J.-W. Yeh, *Surface and Coatings Technology* **2013**, *221*, 118.

[4] P. Sarker, T. Harrington, C. Toher, C. Oses, M. Samiee, J. P. Maria, D. W. Brenner, K. S. Vecchio, S. Curtarolo, *Nat Commun* **2018**, *9*, 4980.

[5] J. Gild, Y. Zhang, T. Harrington, S. Jiang, T. Hu, M. C. Quinn, W. M. Mellor, N. Zhou, K. Vecchio, J. Luo, *Sci Rep* **2016**, *6*, 37946.

[6] J. Gild, J. Braun, K. Kaufmann, E. Marin, T. Harrington, P. Hopkins, K. Vecchio, J. Luo, *Journal of Materiomics* **2019**, *5*, 337.

[7] a) B. Gludovatz, A. Hohenwarter, D. Catoor, E. H. Chang, E. P. George, R. O. Ritchie, *Science* **2014**, *345*, 1153; b) Z. Li, K. G. Pradeep, Y. Deng, D. Raabe, C. C. Tasan, *Nature* **2016**, *534*, 227.

[8] Z. Hemmat, J. Cavin, A. Ahmadiparidari, A. Ruckel, S. Rastegar, S. N. Misal, L. Majidi, K. Kumar, S. Wang, J. Guo, R. Dawood, F. Lagunas, P. Parajuli, A. T. Ngo, L. A. Curtiss, S. B. Cho, J. Cabana, R. F. Klie, R. Mishra, A. Salehi-Khojin, *Advanced Materials* **2020**.

[9] a) M. C. Troparevsky, J. R. Morris, P. R. C. Kent, A. R. Lupini, G. M. Stocks, *Physical Review X* **2015**, *5*, 011041; b) Z. Lun, B. Ouyang, D.-H. Kwon, Y. Ha, E. E. Foley, T.-Y. Huang, Z. Cai, H. Kim, M. Balasubramanian, Y. Sun, J. Huang, Y. Tian, H. Kim, B. D. McCloskey, W. Yang, R. J. Clément, H. Ji, G. Ceder, *Nature Materials* **2020**.

[10] D. B. Miracle, O. N. Senkov, *Acta Mater.* **2017**, *122*, 448.

[11] S. J. Pennycook, D. E. Jesson, *Ultramicroscopy* **1991**, *37*, 14.

[12] W. Zhu, B. A. Rosen, A. Salehi-Khojin, R. I. Masel, *Electrochim. Acta* **2013**, *96*, 18.

[13] M. Asadi, M. H. Motevaselian, A. Moradzadeh, L. Majidi, M. Esmaeilirad, T. V. Sun, C. Liu, R. Bose, P. Abbasi, P. Zapol, A. P. Khodadoust, L. A. Curtiss, N. R. Aluru, A. Salehi-Khojin, *Advanced Energy Materials* **2019**, *9*, 1803536.

[14] W. Zhu, R. Michalsky, Ö. Metin, H. Lv, S. Guo, C. J. Wright, X. Sun, A. A. Peterson, S. Sun, *Journal of the American Chemical Society* **2013**, *135*, 16833.

[15] S. Lin, C. S. Diercks, Y.-B. Zhang, N. Kornienko, E. M. Nichols, Y. Zhao, A. R. Paris, D. Kim, P. Yang, O. M. Yaghi, C. J. Chang, *Science* **2015**, *349*, 1208.

[16] a) P. Abbasi, M. Asadi, C. Liu, S. Sharifi-Asl, B. Sayahpour, A. Behranginia, P. Zapol, R. Shahbazian-Yassar, L. A. Curtiss, A. Salehi-Khojin, *ACS Nano* **2017**, *11*, 453; b) M. Asadi, K. Kim, C. Liu, A. V. Addepalli, P. Abbasi, P. Yasaei, P. Phillips, A. Behranginia, J. M. Cerrato, R. Haasch, P. Zapol, B. Kumar, R. F. Klie, J. Abiade, L. A. Curtiss, A. Salehi-Khojin, *Science* **2016**, *353*, 467; c) B. A. Rosen, A. Salehi-Khojin, M. R. Thorson, W. Zhu, D. T. Whipple, P. J. A. Kenis, R. I. Masel, *Science* **2011**, *334*, 643; d) J. Gu, C.-S. Hsu, L. Bai, H. M. Chen, X. Hu, *Science* **2019**, *364*, 1091.

[17] J. K. Nørskov, J. Rossmeisl, A. Logadottir, L. Lindqvist, J. R. Kitchin, T. Bligaard, H. Jónsson, *The Journal of Physical Chemistry B* **2004**, *108*, 17886.

[18] M. Asadi, B. Kumar, A. Behranginia, B. A. Rosen, A. Baskin, N. Repnin, D. Pisasale, P. Phillips, W. Zhu, R. Haasch, R. F. Klie, P. Král, J. Abiade, A. Salehi-Khojin, **2014**, *5*, 4470.

[19] a) T. A. A. Batchelor, J. K. Pedersen, S. H. Winther, I. E. Castelli, K. W. Jacobsen, J. Rossmeisl, *Joule* **2019**, *3*, 834; b) T. Löffler, H. Meyer, A. Savan, P. Wilde, A. Garzón Manjón, Y.-T. Chen, E. Ventosa, C. Scheu, A. Ludwig, W. Schuhmann, *Advanced Energy Materials* **2018**, *8*, 1802269; c) S. Wang, H. Xin, *Chem* **2019**, *5*, 502.

[20] a) G. Henkelman, B. P. Uberuaga, H. Jónsson, *The Journal of Chemical Physics* **2000**, *113*, 9901; b) G. Henkelman, H. Jónsson, *The Journal of Chemical Physics* **2000**, *113*, 9978.

[21] A. Zunger, S. Wei, L. G. Ferreira, J. E. Bernard, *Phys Rev Lett* **1990**, *65*, 353.

[22] A. van de Walle, M. Asta, G. Ceder, *Calphad* **2002**, *26*, 539.

[23] a) G. Kresse, J. Furthmüller, *Computational Materials Science* **1996**, *6*, 15; b) J. P. Perdew, K. Burke, M. Ernzerhof, *Physical Review Letters* **1996**, *77*, 3865.

[24] Q. Li, L. He, C. Sun, X. Zhang, *The Journal of Physical Chemistry C* **2017**, *121*, 27563.

[25] L. J. Allen, A. J. D′Alfonso, S. D. Findlay, *Ultramicroscopy* **2015**, *151*, 11.

[26] B. D. Forbes, A. V. Martin, S. D. Findlay, A. J. D'Alfonso, L. J. Allen, *Phys. Rev. B* **2010**, *82*, 104103.

[27] a) M. Asadi, B. Kumar, C. Liu, P. Phillips, P. Yasaei, A. Behranginia, P. Zapol, R. F. Klie, L. A. Curtiss, A. Salehi-Khojin, *ACS Nano* **2016**, *10*, 2167; b) A. Ahmadiparidari, S. Fuladi, L. Majidi, S. Plunkett, E. Sarnello, H. Gholivand, Z. Hemmat, S. Rastegar, S. N. Misal, N. Jimenez, P. C. Redfern, J. Wen, T. Li, A. T. Ngo, F. Khalili-Araghi, L. A. Curtiss, A. Salehi-Khojin, *J. Power Sources* **2021**, *491*, 229506; c) L. Majidi, Z. Hemmat, R. E. Warburton, K. Kumar, A. Ahmadiparidari, L. Hong, J. Guo, P. Zapol, R. F. Klie, J. Cabana, J. Greeley, L. A. Curtiss, A. Salehi-Khojin, *Chem. Mater.* **2020**, *32*, 2764; d) L. Majidi, A. Ahmadiparidari, N. Shan, S. N. Misal, K. Kumar, Z. Huang, S. Rastegar, Z. Hemmat, X. Zou, P. Zapol, J. Cabana, L. A. Curtiss, A. Salehi-Khojin, *Adv. Mater.* **2021**, *33*, 2004393.

Figures

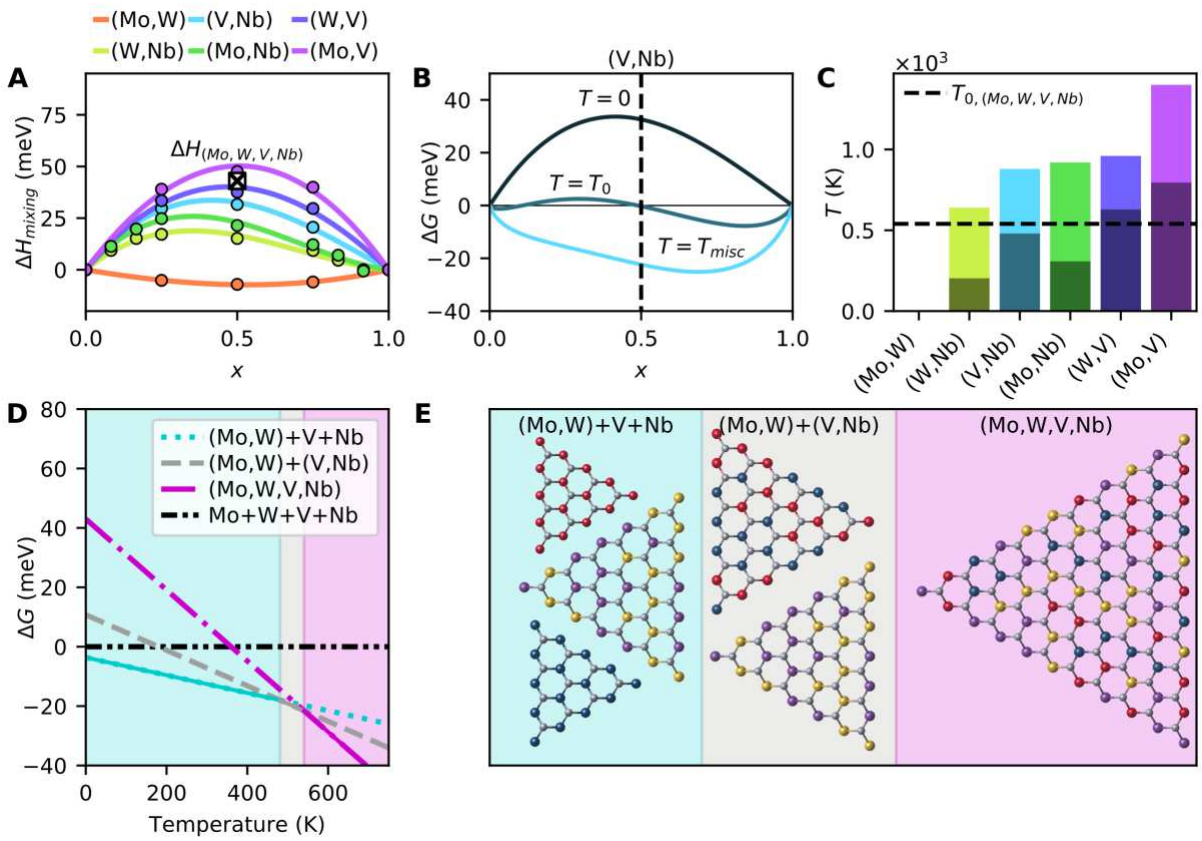

Figure 1. Schematics for the application of the HEA screening technique to (Mo,W,V,Nb). A) The mixing enthalpies for the 6 possible pairwise binary alloys corresponding to (Mo,W,V,Nb) with the boxed x representing the equimolar HEA enthalpy. B) The free energy of (V,Nb) at three temperatures corresponding to 0 K, T_0, and the miscibility temperature. C) The miscibility temperatures of the 6 binary alloys with the greyed portions corresponding to T_0, the temperature where the mixing free energy of the equimolar binary alloy becomes negative. The dashed line corresponds to T_0 for (Mo,W,V,Nb). D) A plot of the equimolar free energy vs temperature for the partial decompositions that are stable at certain temperatures, the HEA and the mixture of individual components for reference. The solid line corresponds to the most stable phase or phase mixture at a particular temperature. E) A diagram showing the decompositions represented in (D).

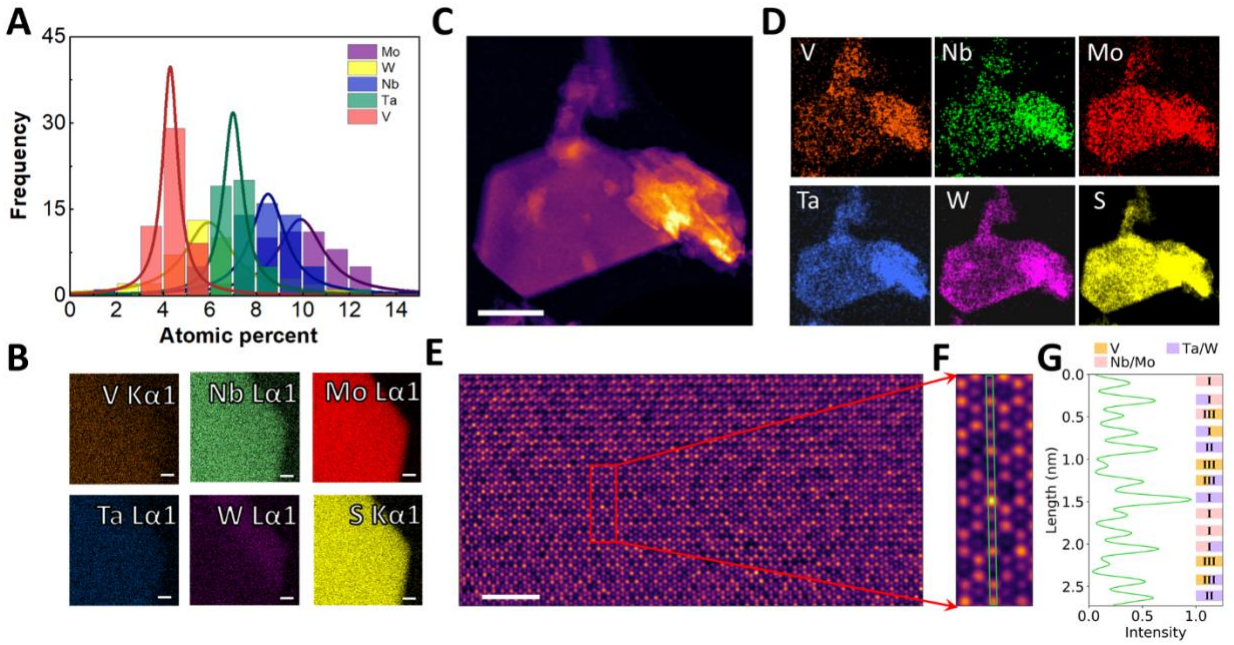

Figure 2. Experimental verification of successful synthesis of the TMDC HEA (Mo,W,V,Nb,Ta). A) Histogram TM stoichiometries from 60 synthesized flakes from SEM-EDX data. B) Elemental mapping EDS data showing a homogeneous spatial distribution of each TM in a representative (Mo,W,V,Nb,Ta) flake. C) STEM-HAADF image showing a typical high entropy TMDC flake. D) EDS chemical maps showing V, Nb, Mo, Ta, W and S distribution for the flake shown in (C). E) STEM-HAADF image of a flake, where the highlighted region (red box) shows the [001] projection of a typical TMDC structure. F) Atomic resolution STEM-HAADF image showing local variations in the intensity of atomic columns due to varying composition of cations. G) Intensity profile of the region illustrated in (F) as green box, where the legends correspond to the predominant elements in each atomic column. Scale bars correspond to 100 nm for (C) and 2 nm for (E).

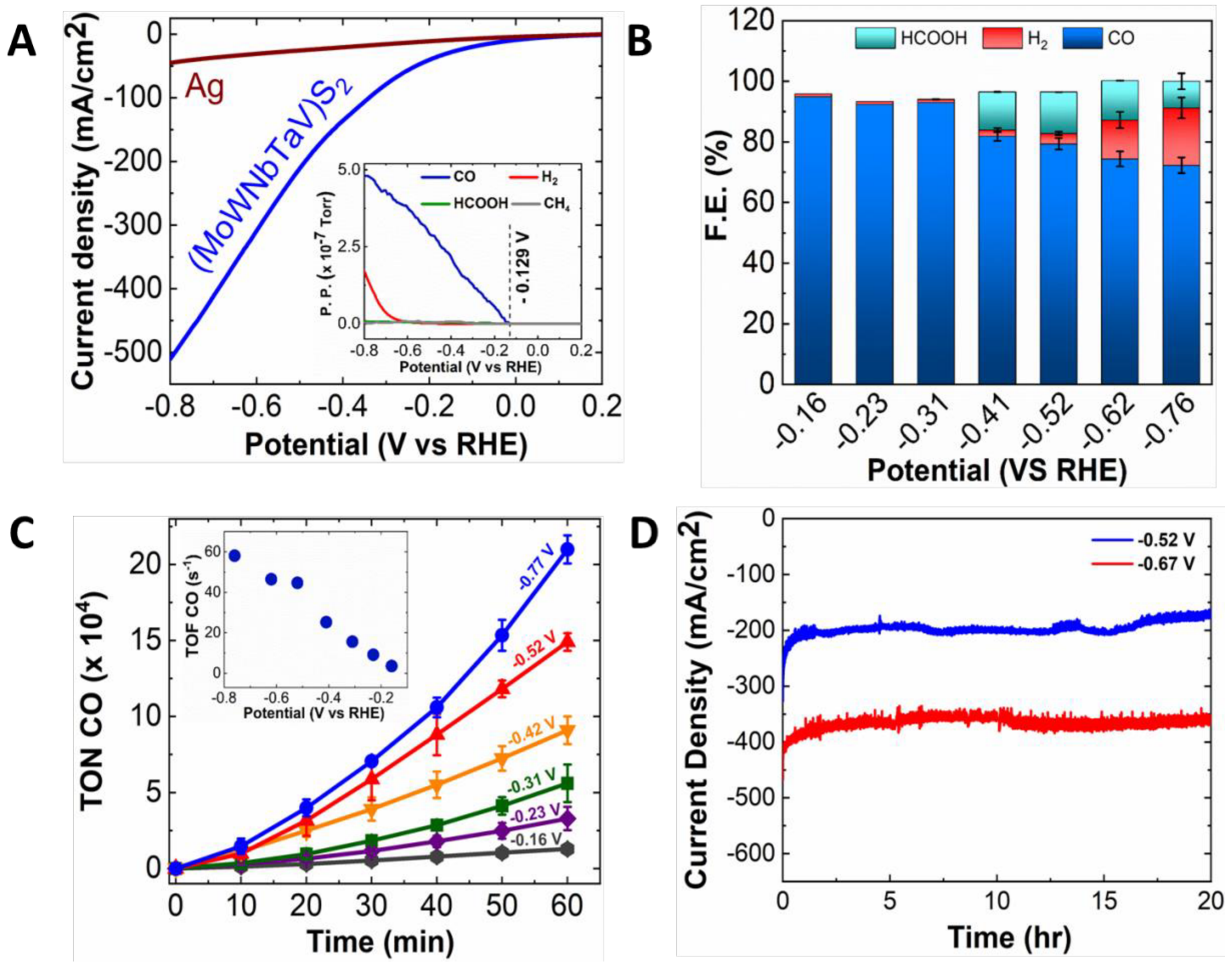

Figure 3. Experimental CO_2RR catalysis results for (Mo,W,V,Nb,Ta). A) The current density of (Mo,W,V,Nb,Ta) and Ag nanoparticles plotted against V vs RHE using LSV with simultaneous measurements of partial pressure of gaseous products in the inset. B) Faradaic Efficiency (F.E.) of CO, H_2 and HCCOH from chronoamperometry experiments using (Mo,W,V,Nb,Ta) NFs at different potentials. The error bars represent the standard deviation of three experiments. C) Turn over numbers (TON) of CO formation over the course of an hour at various voltages with the turnover frequency (TOF) of the CA inset. D) Long-term chronoamperometry experiments (20 hours) at 2 different potentials. Potentials in (C) and (D) are based on RHE.

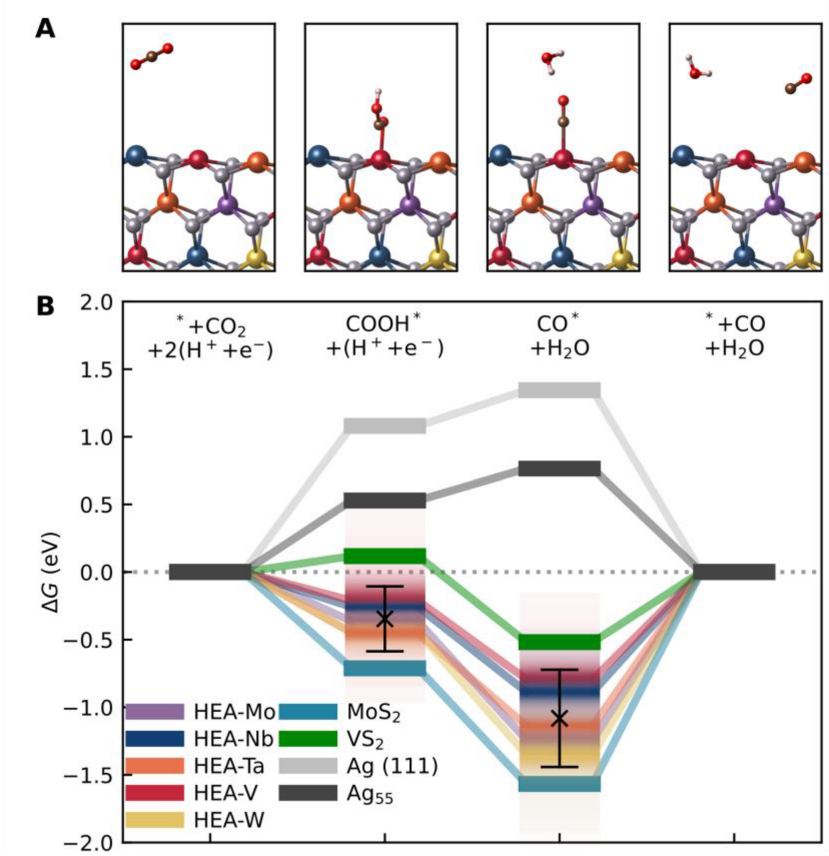

Figure 4. Theoretical catalysis results for the HEA, select pure TMDCs and silver. A) HEA ribbon SQS visualizations at each step of the catalytic reaction with molecules adsorbed to the V site (configuration Ribbon-00). B) Free energy pathway of CO_2 reduction at the equilibrium condition potential. The extent of the spread of each of the HEA free energy lines corresponds to $\pm 2\sigma$, and black x's with error bars correspond to averages and standard deviations taken over all configurations and sites. Unary free energies are also shown for MoS_2, VS_2 and Ag.